Chemical Imaging by Single Pulse Interferometric Coherent Anti-Stokes Raman Scattering Microscopy

Sang-Hyun Lim, Allison G. Caster, Olivier Nicolet, and Stephen R. Leone*

Departments of Chemistry and Physics, University of California at Berkeley and Lawrence Berkeley National Laboratory, Berkeley, California 94720

Received: December 23, 2005

A single pulse interferometric coherent anti-Stokes Raman (CARS) spectroscopy method is used to obtain broadband CARS spectra and microscopy images of liquid and polymer samples. The pump, Stokes, and probe pulses are all selected inside a single broadband ultrafast pulse by a phase- and polarization-controlled pulse shaping technique and used to generate two spectral interference CARS signals simultaneously. The normalized difference of these two signals provides an amplified background-free broadband resonant CARS spectrum over the 400−1500 cm^{-1} range with 35 cm^{-1} spectral resolution. Chemically selective microscopy images of multicomponent polymer and liquid samples are investigated with this new CARS method. Multiplex CARS spectra at 10 000 spatial points are measured within a few minutes, and used to construct chemically selective microscopy images with a spatial resolution of 400 nm. The spectral bandwidth limits, sensitivity, homodyne amplification advantages, spatial resolution, depolarization, chromatic aberration, and chemical imaging aspects of this new technique are discussed in detail.

I. Introduction

Coherent anti-Stokes Raman scattering (CARS) microscopy is a promising chemically selective microscopy technique that uses the vibrational response of the sample molecules themselves as a contrast mechanism, eliminating the need for sample labeling such as fluorescent dyes.[1−3] Moreover, the method allows three-dimensional imaging and has a higher spatial resolution than one- or even two-photon fluorescence due to the nature of the coherent three-photon process.[3,4]

The nonresonant CARS signal is the biggest problem in CARS microscopy because it can obscure the desired resonant CARS signal.[1,5] This background is generated by the electronic response of the sample and is independent of the signal frequency.[1,6,7] It is more problematic in multiplex CARS experiments, because a broadband ultrafast pulse (a shorter pulse in the time domain) is required, and the shorter the pulse duration, the stronger the nonresonant signals become.[1,2,8] On the other hand, it is very desirable to cover a broad CARS spectral window for spectral analysis.[9] The so-called "Raman fingerprint region" spans from 800 to 1800 cm^{-1} for most organic molecules.[10] If one wishes to cover the entire fingerprint window in the previously reported multiplex CARS techniques that use synchronized narrow bandwidth pump and probe pulses together with broad bandwidth Stokes pulses,[2,5] the Stokes pulse needs to have a bandwidth of more than 1000 cm^{-1}. A pulse having this amount of bandwidth generates a huge nonresonant background, which will completely dominate the relatively weak resonant signals.[11,12]

Recently, several groups demonstrated the possibility of extracting resonant CARS signals via interferometry (in both the time and spectral domain).[13−15] Since the resonant and nonresonant signals are coherent and have different responses to the phases of the pump, Stokes, and probe light fields,

interferometry can be used to extract the pure resonant signals.[13,15] In this approach, one can also amplify the CARS signals via a homodyne amplification mechanism, since the detected signal is the cross term between the resonant signal and a local oscillator.[8,13]

Silberberg and co-workers pioneered single-pulse multiplex CARS methods with a pulse shaping technique.[7,11,16−19] This approach greatly simplifies the experimental setup, eliminates the problem of timing jitter between the two pulses, and enables control of the relative phases and polarizations of the resonant and nonresonant CARS signals. With a polarization- and phase-controlled technique, they showed that it is possible to obtain a background-free CARS spectrum.[19]

Recently, we combined the interferometric[13] and polarization/phase control[19] methods to demonstrate a method of single pulse interferometric CARS spectroscopy.[12] We use the pulse shaping technique to generate CARS signals and control the relative phase between the resonant and nonresonant signals to implement a double quadrature spectral interferometry (DQSI)[13,20] technique utilizing the internal nonresonant signal as a local oscillator. This new technique can extract the imaginary and real parts of the background-free resonant CARS spectrum in a single experimental measurement.[12] It not only retrieves the imaginary part of the CARS signal, but also amplifies it significantly, allowing a substantial sensitivity improvement.[12] In this report, we present a more thorough analysis of this technique, quantify the sensitivity, and apply it to obtain chemically selective microscopy images of liquid and polymer samples. Detailed analyses of the CARS signal generation, the double quadrature spectral interferometry (DQSI) method, the experimental setup, homodyne amplification advantages, and chemical imaging aspects are presented. Several issues such as spectral bandwidth limits, signal sensitivity, spatial resolution, sample depolarization, and chromatic aberration are also discussed.

---

* Address correspondence to this author. E-mail: srleone@berkeley.edu.

Chemical Imaging by Interferometric CARS Microscopy

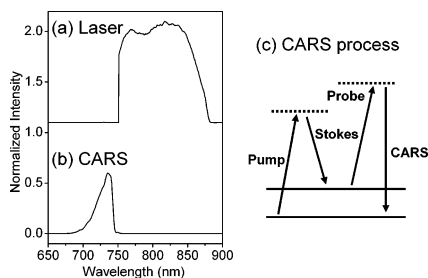*J. Phys. Chem. B, Vol. 110, No. 11, 2006* **5197**

Figure 1. Normalized spectra of (a) the laser pulse and (b) CARS signal generated by the transform-limited (TL) pulse. (c) Energy level diagram of the CARS process.

II. Double Quadrature Spectral Interferometric Coherent Anti-Stokes Raman Scattering (DQSI-CARS) Spectroscopy

In this section, a systematic analysis of the single pulse multiplex CARS signal generation and the double quadrature spectral interferometric CARS (DQSI-CARS) technique is considered. The method is developed to show how a background-free resonant CARS spectrum can be extracted in a single experimental measurement. Briefly, we excite a sample with a single phase/polarization-controlled broadband laser pulse to generate spectral interferometric signal traces along two different polarization directions at the same time. The normalized difference spectrum from the two signals results in the background-free broadband multiplex CARS spectrum, providing vibrational information equivalent to that of spontaneous Raman scattering.

Figure 1a shows the spectrum of the laser pulse used in this experiment. Note that the bandwidth of the laser is more than 120 nm ($\sim$1800 cm^{-1}). The wavelengths of the laser shorter than 750 nm are cut off by a wide variable slit placed after the spatial light modulator inside a pulse shaper. Figure 1b shows the spectrum of the CARS signal from toluene (the sum of both the resonant and nonresonant signals) acquired through a short wave pass filter (to reject the laser pulses) with a transform-limited (TL) pulse.[11] All possible combinations of wavelengths within the bandwidth can be used in principle as the pump, Stokes, and probe pulses (as shown in Figure 1c) to generate the CARS signal, which has a smooth spectral shape with monotonically decreasing intensity at shorter wavelengths (Figure 1b).[11,19] This spectral shape is due to the fact that there are fewer possible frequency combinations of pump, Stokes, and probe pulses to generate the shorter wavelength CARS signals.

With single pulse excitation, the resonant and nonresonant CARS signals can be described by[6,7]

$$P_R(\omega) \propto \int_0^\infty d\Omega\, \chi_R(\Omega) E(\omega - \Omega) A(\Omega) \qquad (1)$$

$$P_{NR}(\omega) \propto \int_0^\infty d\Omega\, \chi_{NR}(\Omega) E(\omega - \Omega) A(\Omega) \qquad (2)$$

where

$$A(\Omega) = \int_0^\infty d\omega'\, E^*(\omega') E(\Omega + \omega') \qquad (3)$$

$$\chi_R(\Omega) \equiv \alpha_R \sum_k \frac{a_k}{(\Omega_k - \Omega) + i\Gamma_k} \qquad (4)$$

$$\chi_{NR}(\Omega) \equiv \alpha_{NR}/\Omega \qquad (5)$$

P_R and P_{NR} are the third order vibrationally resonant and nonresonant transient polarizations, respectively. E is the laser
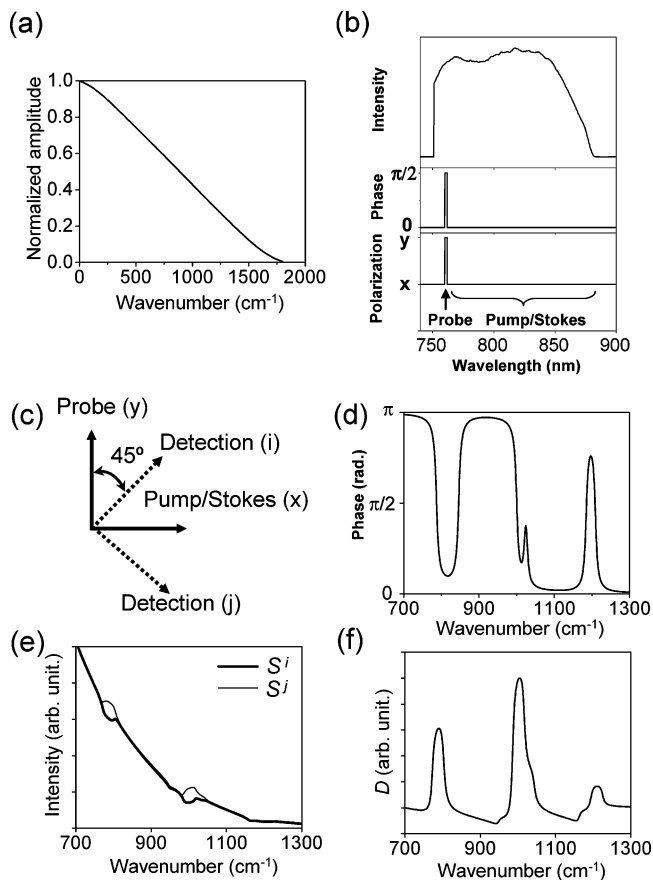

Figure 2. (a) Simulated amplitude spectrum of the coherent vibrational excitation, $A(\Omega)$, with a transform-limited pulse. (b) Intensity, phase, and polarization of the shaped laser pulse used in DQSI-CARS. (c) Polarization directions of pump/Stokes (x), probe (y), and detections (i and j). (d) Phase spectrum calculated for toluene. (e) Simulations of the two signal spectra (S^i and S^j) for toluene with eqs 1−5, and 11. (f) The normalized difference spectrum (D) according to eq 13 from the two simulated signal traces in part e.

field, and Ω and ω are the frequencies of the coherent vibrational excitation and CARS signals, respectively. χ_R is the vibrationally resonant third-order susceptibility, and a_k, Ω_k, and Γ_k are the relative intensity, energy, and line width of vibrational mode k, respectively. χ_{NR} is the vibrationally nonresonant susceptibility, which generates the nonresonant CARS signals. α_R and α_{NR} are the amplitude coefficients of the resonant and nonresonant susceptibilities, respectively, responsible for the wavelength independent factors such as concentration, electronic polarizability, etc. Note that α_{NR}/α_R determines the relative intensity ratio between the nonresonant and resonant CARS signals. $A(\Omega)$ corresponds to the coherent vibrational excitation generated by the pump and Stokes pulses.[7] The calculated spectrum of $A(\Omega)$ with a TL pulse, in Figure 2a, has monotonically decreasing intensities versus higher vibrational frequency of the resulting CARS signals. This quantity will determine both the CARS spectral window and peak intensity distribution since the spectral distributions of the resonant vibrational CARS signals are a convolution of $A(\Omega)$, the probe electric field, and the third-order vibrational susceptibility (χ_R) as shown in eq 1.[7]

To obtain a multiplex CARS signal, it is necessary to separate out a spectrally narrow probe pulse.[19] We select the probe pulse by the phase/polarization mask shown in Figure 2b. The probe width is chosen to be two pixels, which corresponds to 30 cm^{-1} bandwidth. The polarization directions of the pump/Stokes pulses and the probe pulse are along the x- and y-directions, respectively (Figure 2c). For simplicity, we begin with an

5198 *J. Phys. Chem. B, Vol. 110, No. 11, 2006*

Lim et al.

assumption that the line width of the probe (selected by the phase and polarization-mask shown in Figure 2b) is spectrally much narrower than the vibrational line width (Γ_R). Consider the case where the phase of the probe pulse is set to $\pi/2$. Then, the electric fields of the laser along x- and y-polarization directions become

$$E^y(\omega) \approx E_{Pr}\delta(\omega - \omega_{Pr})\exp(i\pi/2) = iE_{Pr}\delta(\omega - \omega_{Pr}) \quad (6)$$

$$E^x(\omega) = E(\omega) - E^y(\omega) \approx E(\omega) \quad (7)$$

where E^y and E^x are the electric fields of the laser pulse along the y- and x-polarization directions. E is the amplitude of the total electric field, i.e., $E = |\vec{E}| = |E^x\hat{x} + E^y\hat{y}|$, where $\hat{x}$ and $\hat{y}$ are the unit vectors along x and y directions, respectively. δ is the delta function, ω_{Pr} is the frequency of the probe pulse, and E_{Pr} is the field intensity at the frequency of the probe pulse (ω_{Pr}), respectively. Note that E_{Pr} is a constant, not a function of frequency. Also note that most of the laser pulse energy is in the x-direction (eq 7).

The resulting resonant CARS signals along x- and y-directions are described by

$$P_R^x(\omega) = \int_0^\infty d\Omega\, \chi_R(\Omega)E(\omega - \Omega)A(\Omega)$$

$$P_R^y(\omega) = \int_0^\infty d\Omega\, \chi_R(\Omega)i\delta(\omega - \Omega - \omega_{Pr})E_{Pr}A(\Omega) = \\ i\chi_R(\Omega)E_{Pr}A(\omega - \omega_{Pr}) \quad (8)$$

Since the nonresonant signal with a short pulse laser used in this experiment (pulse duration ∼10 fs) is orders of magnitude larger than the resonant signal and polarized along the x-direction, the total transient polarizations along the x- and y-polarization directions become

$$P^x(\omega) = P_{NR}(\omega) + P_R^x(\omega) \approx P_{NR}(\omega)$$

$$P^y(\omega) \approx P_R^y = i\chi_R(\omega - \omega_{Pr})E_{Pr}A(\omega - \omega_{Pr}) \quad (9)$$

As one can see in eq 9, the spectrally resolved resonant CARS signals (P^y) can be separated from the nonresonant signals (P^x) by the polarization directions. The y-polarized signal, i.e., the spectrally resolved resonant CARS signal, is what one wishes to measure in the experiment. Note that P^x is a real quantity, and P^y is a complex one (χ_R is a complex function while χ_{NR} is a real one).

One can selectively detect the spectrally resolved resonant signals by eliminating the nonresonant signals (P^x) with a polarizer, which was demonstrated by Silberberg and co-workers.[19] We adopt a different approach here.[12] If the CARS signals are detected along a polarization direction other than the x-polarization direction (Figure 2c), the resulting signals are a coherent sum of the nonresonant (P^x) and resonant signals (P^y). The x- and y-polarized CARS signals are coherent and have characteristic phase relationships with respect to the phases of the pump/Stokes and probe laser fields. As mentioned above, the x-polarized signal is mostly the nonresonant signal and has a flat phase function over all signal frequencies. Note that even the resonant component of the CARS signal along the x-polarization direction (P_R^x) has a smooth, almost flat phase function, since there is no spectrally narrow probe pulse in this polarization direction. Therefore we can use this signal as a local oscillator. In contrast, the y-polarized signal (P^y) is the spectrally resolved resonant CARS signal. It has a π phase shift at every vibrational resonance frequency, resulting in a nonflat phase

spectrum over the signal frequencies. Figure 2d shows such a phase spectrum calculated for toluene. The spontaneous Raman spectrum of toluene is used for the relative peak intensities and vibrational peak positions in the simulation of Figure 2d, as described further below. When the x- and y-polarized signals are added together in a polarization direction other than the x- and y-axes, the detected signal has a modulated interference pattern at every vibrational resonance frequency since constructive and destructive interferences occur at each vibrational resonance, where the resonant signal has a π phase shift. We can also control the interference pattern by controlling the relative phase between the pump/Stokes and probe pulses. Thus the spectral interferometry uses the nonresonant signal as a phase-controllable local oscillator. We developed this new double quadrature spectral interferometry (DQSI) technique[12] to extract the imaginary part of the amplified resonant signals, since this technique can be performed in a single data acquisition without scanning the spatial light modulator (SLM). Next we show the case where the imaginary part of $\chi_R(\omega)$ is extracted; one can also obtain the real part by using a different probe phase, as demonstrated previously, and is not discussed here.[12]

Consider the signals along the $\pm45°$ polarization directions relative to the x-axis (i- and j-directions shown in Figure 2c). The transient third-order polarizations along these polarization directions are

$$P^i(\omega) = \frac{P^x(\omega) + P_R^y(\omega)}{\sqrt{2}}$$

$$P^j(\omega) = \frac{P^x(\omega) - P_R^y(\omega)}{\sqrt{2}} \quad (10)$$

The detected signal photons along the i- and j-polarization directions become

$$S^i(\omega) = |P^i(\omega)|^2 = \frac{1}{2}|P^x(\omega)|^2 + \frac{1}{2}|P^y(\omega)|^2 + \\ \frac{1}{2}P^x(\omega)(P^y(\omega) + P^{y*}(\omega))$$

$$S^j(\omega) = |P^j(\omega)|^2 = \frac{1}{2}|P^x(\omega)|^2 + \frac{1}{2}|P^y(\omega)|^2 - \\ \frac{1}{2}P^x(\omega)(P^y(\omega) + P^{y*}(\omega)) \quad (11)$$

Figure 2e shows numerical simulations of S^i and S^j for toluene. Details of this simulation will be discussed in section IV.

The difference between these two signal traces leads to

$$S^j(\omega) - S^i(\omega) = -P^x(\omega)(P^y(\omega) + P^{y*}(\omega)) \\ = -P^x(\omega)A(\omega - \omega_{Pr})E_{Pr}\{i\chi_R(\omega - \omega_{Pr}) - \\ i\chi_R^*(\omega - \omega_{Pr})\} \\ = 2P^x(\omega)A(\omega - \omega_{Pr})E_{Pr}\,\text{Im}[\chi(\omega - \omega_{Pr})] \quad (12)$$

As one can see in the result of eq 12, $S^j - S^i$ contains the imaginary part of the resonant CARS signal (i.e., $A(\omega - \omega_{Pr})E_{Pr}\,\text{Im}[\chi(\omega - \omega_{Pr})]$) multiplied by P^x, which is the local oscillator (nonresonant CARS signal) that has orders of magnitude larger amplitude. Thus the resonant signal is amplified and the imaginary part of the third-order vibrational susceptibility can be obtained.
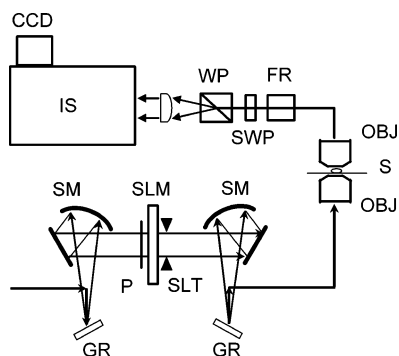
Chemical Imaging by Interferometric CARS Microscopy

J. Phys. Chem. B, Vol. 110, No. 11, 2006 **5199**

Figure 3. Experimental setup: GR, grating; SM, spherical mirror; P, polarizer; SLM, dual bank liquid crystal spatial light modulator; SLT, slit; OBJ, microscope objective; S, sample on the XY piezo stage; FR, Fresnel rhomb (achromatic half wave plate); SWP, sharp edge short wave pass filter; WP, Wollaston prism; and IS, imaging spectrometer.

The absolute amplitude of the nonamplified resonant signal can also be obtained by the following normalized difference

$$
\begin{aligned}
D(\omega) &= \frac{S^i(\omega) - S^j(\omega)}{\sqrt{S^i(\omega) + S^j(\omega)}} = \\
&\frac{2P^x(\omega)A(\omega - \omega_{Pr})E_{Pr}\,\mathrm{Im}[\chi(\omega - \omega_{Pr})]}{\sqrt{|P^x(\omega)|^2 + |P^y(\omega)|^2}} \approx \\
&\frac{2P^x(\omega)A(\omega - \omega_{Pr})E_{Pr}\,\mathrm{Im}[\chi(\omega - \omega_{Pr})]}{P^x(\omega)} = \\
&2A(\omega - \omega_{Pr})E_{Pr}\,\mathrm{Im}[\chi(\omega - \omega_{Pr})] \quad (13)
\end{aligned}
$$

The unit of this new scale (D) is $\sqrt{\text{counts}}$, which corresponds to the field amplitude of the signal. Figure 2f shows the normalized difference spectrum (D in eq 13) from the two simulated traces in Figure 2e.

Two approximations have been used to derive eq 13. The first is that the bandwidth of the probe pulse is much narrower than the line width of the vibrational peak, and the second is that the nonresonant signals are much larger than the resonant signals. In section IV, we will investigate the validity of these two approximations and show how the experimental line shape can be affected if they are no longer valid.

III. Experimental Section

CARS signals are generated with a broadband Ti:Sapphire oscillator (MTS, KM Lasers). The repetition rate of the laser is 90 MHz. The oscillator is optimized to have the broadest bandwidth ($\sim$120 nm as shown in Figure 1a) by carefully adjusting the prism pairs inside the cavity. Figure 3 shows the experimental setup. The pulse is controlled by an all reflective 4f pulse shaper, using a 128 pixel dual bank liquid crystal spatial light modulator (LC-SLM256, CRI). The pulse shaper is configured to control both the phase and polarization of the individual frequency pixels at the Fourier plane by removing the exit polarizer. The 120 nm bandwidth ($\sim$1800 cm^{-1}) of the laser spectrum is encompassed by the pulse shaper. To block the wavelengths outside the controlled part of the pulse, a wide variable slit is installed after the SLM. The shaped pulse is focused into the sample and the signal is collected, using two high N.A. water immersion IR objectives (1.2 and 1.0 N.A., respectively, Olympus). All the signals with various phase matching angles inside the wide focusing angle ($\sim$128° with the 1.2 N.A. water objective) are generated and collected within the tight focusing geometry. Note that the phase matching

conditions for the resonant CARS signal and the local oscillator (nonresonant signals) are exactly the same since they are both generated from the same laser pulse. Comparing the laser spectrum before the focusing objective and after the collecting objective, we do not find any significant transmission irregularity of the microscope objectives used here. The collected signal is rotated by 45° with respect to the x-direction by an achromatic half wave plate (Fresnel Rhomb, CVI) and filtered by a sharp edge short wave pass filter (740ASEP, Omega Optical). The i- and j-polarization signals (as shown in Figure 2c) are separated spatially by a Wollaston prism (CVI), and the two vertically displaced signal beams are coupled to an imaging spectrometer (750si, Chromex) and imaged onto a two-dimensional CCD (DV401-FI, Andor) as two horizontal lines.

The chirp structure of the pulse at the sample position is characterized with the multiple intrapulse interference phase scan (MIIPS) method developed by Dantus and co-workers.[21] Briefly, a cosine phase mask is applied on the SLM and the second harmonic generation (SHG) spectra from a BBO crystal at the sample position are measured while scanning the phase offset of the cosine phase mask. This results in two-dimensional plots having multiple lines, where the TL pulse shows evenly spaced parallel straight lines. A 10 μm thick BBO crystal (Casix) is used to generate the SHG spectra at the sample position on top of a 180 μm thick glass coverslip and water (between the glass coverslip and the focusing objective). A 0.54 N.A. dry objective collects the SHG signals and a fiber-coupled spectrometer (FL2000USB, Ocean Optics) is used to measure the SHG spectra. A phase mask having a phase modulation given by

$$
\phi(\omega) = \alpha\cos(\gamma(\omega - \omega_0) - \delta) \quad (14)
$$

is applied on the SLM, where α is set to 2π, and $2\pi/(1800$ cm^{-1}) is used for γ. γ is chosen to have a one cycle of the cosine phase curve over the full spectrum of the laser. ω_0 is the center frequency of the laser spectrum. The second harmonic generation spectra are taken while the phase offset (δ) is scanned from 0 to 4π.

Panels a and b of Figure 4 show the MIIPS plots of transform-limited (Figure 4a) and chirped (Figure 4b) pulses, respectively. The TL pulse shows evenly spaced parallel lines in the MIIPS plot (Figure 4a). Any deviation from this pattern can be related to the phase structure of the uncompressed pulse.[21] The MIIPS of an uncompressed pulse shows that the neighboring lines are not equally spaced, nor are they parallel to each other (Figure 4b). The different spacing between the nearby lines corresponds to the quadratic phase modulation (ω^2 term), and the different linear slopes of these lines relates to the cubic phase modulation (ω^3 term) of the chirp structure. Higher order chirp structure can also be analyzed by considering the differing higher order curvatures between the neighboring lines in the MIIPS plot.

The MIIPS technique is reliable, easy to use, and gives more information about the pulse phase characteristics than conventional techniques such as SHG autocorrelation or frequency-resolved optical gating (FROG).[22] In microscopy, MIIPS is a preferred pulse characterization technique since the noncollinear FROG is very difficult to set up with a high N.A. microscope objective. The pulse for CARS microscopy needs to be compressed not only in the linear but also in higher order chirp terms. We find that it is important to compress the pulse at least up to the cubic chirp (ω^3 term) to generate the optimum CARS signal.

Another problem encountered during the implementation of the DQSI-CARS is the different spectral responses of the spectrometer between P- and S-polarized signals. This is due
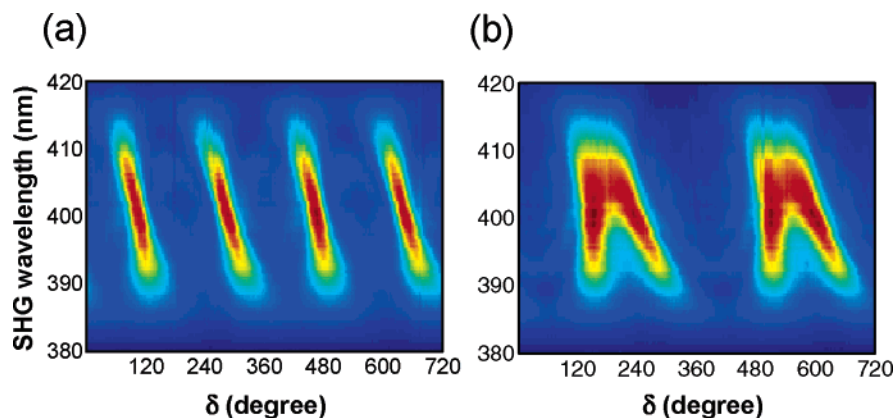
Figure 4. Experimental MIIPS plots of (a) transform-limited (TL) and (b) uncompressed pulses measured at the sample position of the microscope. Note that a TL pulse shows equally spaced parallel lines in panel a. The spacing and different slopes between the lines correspond to the quadratic (ω^2) and cubic (ω^3) phase modulations of the laser pulse, respectively.

to the different reflective response of the grating used in the spectrometer, and we find that it also depends on the optical coupling of the signals to the spectrometer, which can change with different experiments. These effects are calibrated by acquiring CARS signals (S^i and S^j) with the TL pulse as references. Since the S^i and S^j should be exactly the same in this case, normalization of each CCD trace with the CARS reference (the signal with TL pulse) compensates for the different polarization response of the spectrometer. This procedure has to be done only once with each sample.

A CCD exposure time of 10 ms is used here for all the CARS data in both the spectroscopy and microscopy experiments. The time of 10 ms is chosen as representative of the desirable scan time per spatial location (pixel) in a microscopy image, since this is the fastest scan speed of the CCD used here. In the CARS spectroscopy of solvents and solutions, an average laser power of 40 mW before the focusing objective is used. With this power level, we estimate that the power density at the focus is approximately 10^{12} W/cm^2 per pulse assuming a diffraction-limited spot size and 10 fs pulse duration. For microscopy experiments with liquid and polymer samples, the laser power is reduced to 3 mW to prevent sample damage during scanning of the sample.

Spectroscopy experiments are performed with a small drop of the sample sandwiched between two microscope coverslips. The two signal traces (S^i and S^j) are measured and processed according to eq 13 in real time.

In the microscopy experiments, S^i and S^j are acquired with a so-called "multi-track mode" of a two-dimensional CCD. We integrate (bin) the vertical pixels into two different regions corresponding to S^i and S^j. This mode of the CCD operation allows two vertically displaced signal traces to be measured in a fast single readout process. The CCD is cleared after each 10 ms data acquisition, and the data are transferred to a computer and processed in real time. The readout time for a single multitrack scan is also about 10 ms. The sample is scanned by an XY piezo stage (P-733.2CL, PI) synchronized with the CCD acquisition. In this report, all the images consist of 100 pixels × 100 pixels with 0.2 and 0.4 μm step sizes for the amide/PDMS and PS/PMMA images, respectively. The raw data consist of a three-dimensional matrix of CARS spectra at each two-dimensional (2D) spatial point times the number of points in the 2D scans, and the signal traces (S^i and S^j) are also saved for further analysis. The total experiment time for an image with 100 × 100 pixels is about 3.5 min with 10 ms CCD exposure time for each pixel. This includes the CCD exposure time, readout time, and data-processing time. With the laser

repetition rate of 90 MHz, the number of laser pulses used for the CARS spectral measurement of a single spatial spot is 9 × 10^5 with the 10 ms CCD exposure.

A poly(dimethylsiloxane) (PDMS) pattern is made by a soft lithographic technique, using a TEM copper grid as a template.[23] A TEM grid (SPI) is attached to a clean glass substrate with a drop of methanol and dried. A 10:1 mixture (weight percent) of the elastomer base and curing agent from a PDMS elastomer kit (Sylgard 184, Dow Corning) is poured onto the TEM grid on top of the glass substrate. After curing in an oven at 80 °C for about 1 h, the PDMS elastomer pattern (mould of the TEM grid) is peeled off with tweezers. A drop of *N,N*-dimethylformanide (Aldrich) is sandwiched between the PDMS pattern and a microscope coverslip. Polystyrene (PS) and poly(methyl methacrylate) (PMMA) samples are purchased from Aldrich and used as received. A 1:1 mixture (weigh percent) of polymer powders is dissolved in chloroform. A PS/PMMA film is prepared by spin-casting a PS/PMMA solution on a glass coverslip at 600 rpm until the chloroform is dried out. The sample thickness is around 2 μm, which is measured at a razor scratch of the film with an atomic force microscope (AFM).

IV. Results and Discussion

Panels a and b of Figure 5 are experimental signal traces of S^i and S^j for toluene liquid and the corresponding DQSI-CARS spectrum processed according to eq 13. One can see that the experiments match the simulations (Figure 2e,f) reasonably well. We calculated the traces in Figure 2e,f using the E-fields of the entire shaped laser pulses along the i- and j-directions separately using eqs 1−5, 11, and 13. In this way, signal traces can be simulated without any approximation. The spontaneous Raman spectrum of toluene is used to obtain the values of a_k, Ω_k, and Γ_k for four different vibrational peaks (resonances at 788, 1001, 1028, and 1210 cm^{-1}, with relative peak intensities, α_k, of 5, 10, 2.5, and 2, respectively). $\Gamma = 10$ cm^{-1} is used for the line width of all four vibrational peaks. However, the probe spectral width is taken to be 30 cm^{-1} in the simulation, which corresponds to the two pixel width of the probe selected by the SLM. A value of $\alpha_{NR}/\alpha_R = 500$ is used, as discussed further below. This value is chosen to match the experimental interference modulation of the 788 cm^{-1} peak.

As one can see in the simulation in Figure 2f, the resulting DQSI-CARS spectrum has a line shape of the predicted imaginary part of χ_R, but convoluted with the probe pulse shape corresponding to the bandwidth of two pixels (30 cm^{-1}) in the SLM. So the failure of the first approximation (narrow probe
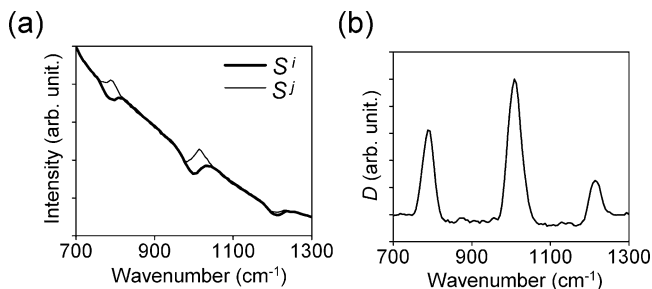
Figure 5. (a) Experimental two-signal spectra (S^i and S^j) and (b) the normalized difference spectrum (D) for toluene.
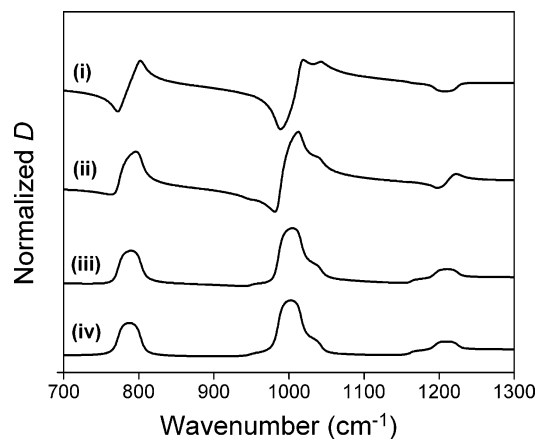

Figure 6. Effect of the resonant CARS signal generated from the pump/Stokes region of the pulse. The toluene vibrational spectrum is used in the simulation. (i) $\alpha_{NR}/\alpha_R = 0$, (ii) $\alpha_{NR}/\alpha_R = 100$, (iii) $\alpha_{NR}/\alpha_R = 500$, and (iv) $\alpha_{NR}/\alpha_R = 10000$. The experimental observations with toluene correspond best to the situation of (iii).

approximation) leads only to a broadening of the spectral line widths of the vibrational peaks.

The only unknown parameter in the simulations of Figure 2e,f is the relative amplitude ratio of the nonresonant and resonant third-order susceptibilities (α_{NR}/α_R). This value can be estimated by comparing the modulated interference depth of the simulation (Figure 2e) and the experiment (Figure 5a). The experimental interference modulation depth at 788 cm^{-1} for toluene is ~10% in the normalized difference of ($S^j - S^i$)/($S^j + S^i$) and $\alpha_{NR}/\alpha_R = 500$ is found to generate this amount of modulation within 10% error. This ratio validates the second approximation ($P_{NR} \gg P_R$). We investigate the effect of this approximation below by simulating several CARS line shapes with different α_{NR}/α_R values and comparing simulation results with the experiment.

With a broadband pulse like the one used in this experiment, the nonresonant signal is at least an order of magnitude greater than the resonant signal in most condensed phase samples.[11] We use the *x*-polarized signals (P^x) as a local oscillator to perform spectral interferometry. The local oscillator, however, is not only from the nonresonant signal.[11] It also contains broadband resonant CARS signals (P_R^x in eq 8) from any possible pump, Stokes, and probe pulse wavelength combinations within the pump/Stokes region of the laser spectrum (Figure 2b). This resonant CARS signal (P_R^x) has a smooth spectral shape because there is no sharp phase or polarization structure in the laser pulse. This signal (P_R^x), however, will change the phase relationship in the interferometry. If we take this effect into account, the local oscillator becomes (P^x)

$$P^x(\omega) = P_{NR}^x(\omega) + P_R^x(\omega)$$

$$= \alpha_{NR}\int_0^\infty d\Omega/\Omega \, E^x(\omega - \Omega)A(\Omega) +$$

$$\alpha_R\int_0^\infty d\Omega \sum_k \frac{a_k}{(\Omega_k - \Omega) + i\Gamma_k} E^x(\omega - \Omega)A(\Omega)$$

$$\equiv |P^x| \exp(i\phi_{LO}(\omega)) \qquad (15)$$

Here we use eqs 1−5 without any assumptions. Note that P_{NR}^x is a real quantity, and P_R^x is a complex one since it contains an integration of the complex Lorentzian line shape function. In the time domain, it can also be understood such that P_R^x contains the effect of vibrational decoherence, which is manifested as a complex Lorentzian function in the frequency domain. Also note that the phase spectrum of P_R^x is smooth and mostly flat because there are no sharp phase features in E^x and $A(\Omega)$. Thus, the local oscillator (P^x) becomes a complex quantity having a smooth phase spectrum ($\phi_{LO}(\omega)$) instead of a zero phase value. The ratio of α_{NR}/α_R determines how much the phase of the local oscillator is shifted from zero in the

simulation. In the case of $\alpha_{NR} \gg \alpha_R$, P^x becomes P_{NR}^x, and $\phi_{LO}(\omega) = 0$. This is the assumption we used previously.

However, if there is a significant amount of P_R^x in P^x (i.e., $\alpha_{NR} \gg \alpha_R$ is no longer valid), the interferometry will be modified by the sample-dependent P_R^x (thus $\phi_{LO}(\omega)$, too). We can simulate this effect by comparing the calculations of different α_{NR}/α_R values. Figure 6 shows the simulated CARS spectra for four different α_{NR}/α_R values using the toluene spectra as a model. One can see that the nonpure local oscillator will distort the DQSI-CARS spectral shape in the case of (i) {$\alpha_{NR}/\alpha_R =0$, resonant signal only} and even up to (ii) {$\alpha_{NR}/\alpha_R =100$}. By comparing the interference modulation depth in the simulated S^i and S^j traces with a given α_{NR}/α_R value, one can simulate the experimental α_{NR}/α_R ratio for the sample. In most samples, we find that this ratio is large enough to generate a reasonable spectral shape. In toluene, the ratio between the nonresonant and resonant signals is one of the smallest among condensed phase samples ($\alpha_{NR}/\alpha_R \sim 500$, (iii)), but this is still large enough to generate a reasonable spectral line shape compared to the almost pure nonresonant local oscillator case ($\alpha_{NR}/\alpha_R \sim 10\,000$, (iv)). In the case of biological samples, the ratio of α_{NR}/α_R will be at least an order of magnitude larger than that for toluene, so the interferometric technique can be applied to most materials and biological imaging problems.

Next we explain that even if there is a significant amount of relative broadband resonant signal (P_R^x) in the local oscillator, the resulting DQSI-CARS spectral peak shape becomes a mixture of imaginary and real parts of a Lorentzian line shape function i and ii in Figure 6. By replacing eq 9 with eq 15, one can show that eq 12 leads to

$$S^j(\omega) - S^i(\omega) = 2|P^x(\omega)|A(\omega - \omega_{Pr})E_{Pr}\{Im[\chi_R(\omega -$$

$$\omega_{Pr})]\cos\phi_{LO}(\omega) - Re[\chi_R(\omega - \omega_{Pr})]\sin\phi_{LO}(\omega)\} \quad (16)$$

So if the local oscillator is contaminated by P_R^x, it will distort the CARS line shape to be a mixture of imaginary and real parts of a Lorentzian function. We can correct this distortion by adjusting the probe phase to cancel the effect of $\phi_{LO}(\omega)$ or use the distorted spectrum as a contrast mechanism to be interpreted by a numerical fitting process.[2]

Thus far we described the theoretical aspects of the interferometric CARS technique. Next we show experimental results and discuss several aspects in both the spectroscopy and microscopy imaging with this technique.
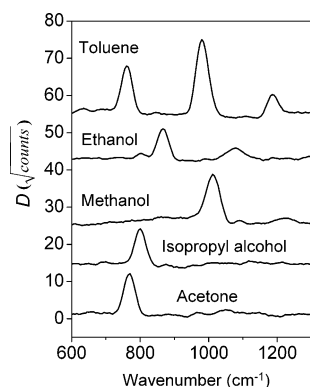
Figure 7. DQSI-CARS spectra of common lab solvents. Each trace is displaced vertically for clarity. Note that the data are taken with the microscope set up with 10 ms CCD exposure time.

Figure 7 shows the experimental DQSI-CARS spectra of several common lab solvents taken with a CCD exposure time of 10 ms. The spectra are processed from the two simultaneously measured signals (S^i and S^j) according to eq 13. The currently accessible CARS window is from 400 to 1500 cm^{-1}, although the signal decreases rapidly beyond 1200 cm^{-1}. The lower limit comes from rejection of the signal by the short wave pass filters used to block the laser. The higher limit is from the limited bandwidth of the laser spectrum. Although we have ~1800 cm^{-1} of laser bandwidth, the CARS signal intensity at a given frequency is proportional to the available combinations of the pump and Stokes pulse that have frequency differences at the CARS signal frequency. So the signal intensity is proportional to the square of the coherent excitation spectrum $A(\Omega)$ in eq 3. There is, however, another limiting factor. To generate higher frequency signals, two pulses with greater frequency differences have to be focused at the sample. Axial chromatic aberration (ACA) will cause the different color components of the laser pulses to focus at different axial positions, which translates to less spatial overlap between pump and Stokes pulses for the higher frequency CARS signals. We verified the effect of ACA qualitatively by comparing experiments using different microscope objectives with different ACA.

The spectral resolution is ~35 cm^{-1}, which is a little broader than the two pixel width of the SLM (30 cm^{-1}) that defines the probe width (Figure 2b). The vertical scale in Figure 7 is the normalized difference D defined by eq 13. This scale (the units are $\sqrt{counts}$) corresponds to the field intensity of the nonamplified resonant CARS signal (note that the square of the field is equivalent to the photon counts). For example, the 1001 cm^{-1} peak of the toluene has ~20 $\sqrt{counts}$, so the actual resonant signal has ~400 counts in 10 ms. However, the signal-to-noise ratio is enhanced because of the homodyne amplification by the nonresonant signal.[12]

Figure 8 shows the sensitivity achieved thus far by the DQSI-CARS method. The samples are ~1 M sulfite, phosphate, and nitrite solutions in water, which have an order of magnitude less signal than the solvents shown in Figure 7. We estimate the number of molecules in the excitation volume (~40 aL) is around 40 attomoles (~2 × 10^7 molecules). The experimental conditions are exactly the same as in Figure 7. The nonamplified resonant CARS signal intensities ($|P_R^y|^2$) for these samples are just a few counts in the 10 ms experiment time, whereas the CCD readout noise is close to the actual peak signal level shown in Figure 8. Note that the signal-to-noise ratio (S/N) in Figure 8 is much greater than would be possible by detecting the nonamplified resonant signals with instrumental noise. Although the scale (D) shows the signal intensities quantitatively (note
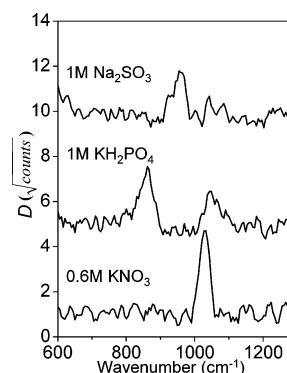

Figure 8. DQSI-CARS spectra of nitrite, phosphate, and sulfite solutions in water. The CCD exposure time is 10 ms. Each trace is displaced vertically for clarity.
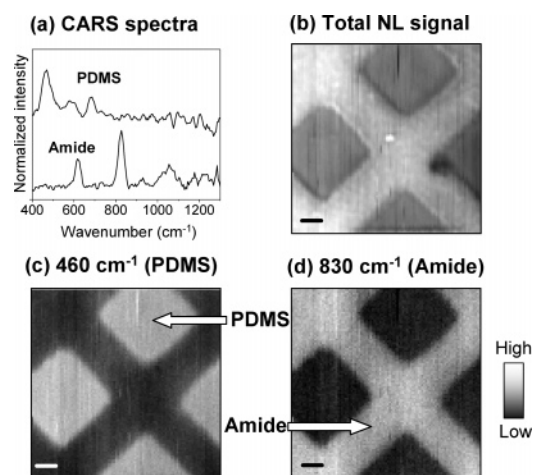

Figure 9. Chemical imaging of amide (*N,N*-dimethylformamide) inside a PDMS (poly(dimethylsiloxane)) template. (a) DQSI-CARS spectra of the amide and PDMS. (b) Image of the total nonlinear (NL) signal integrated over 400−1500 cm^{-1}. (c and d) Images constructed with peaks at (c) 460 cm^{-1} (PDMS) and (d) 830 cm^{-1} (amide), respectively. The scale bar is 2 μm. The pixel size in the image is 200 nm × 200 nm. Note that these images are constructed from a single experimental scan, where each pixel in the image contains the complete spectrum from 400 to 1500 cm^{-1}.

that vertical traces are displaced for clarity in Figures 7 and 8), the signal-to-noise ratio (S/N) is improved significantly. The background noise here is mostly from the shot noise of the signal traces (S^i and S^j), which is orders of magnitude greater than the resonant signal. We verify this by comparing a theoretical shot noise calculation with the experiment. In a previous publication, we also showed that such samples would be difficult to measure with the original phase- and polarization-controlled CARS technique.[12]

If the sample has distinct CARS marker peak(s), which is the case for the PDMS/ *N,N*-dimethylformamide (we refer to this as amide from now on) sample shown in Figure 9, the distinguishing vibrational band can be used for chemical imaging.[3] Figure 9a shows the measured DQSI-CARS spectra of PDMS and amide. Here we use the 460 and 830 cm^{-1} peaks as separate markers for PDMS and amide, respectively, because these two peaks are isolated and distinctly characteristic of the two chemicals in the sample. Figure 9b first shows an image with a contrast that we call a "total nonlinear (NL) signal". If we integrate the raw data traces (S^i and S^j) from 400 to 1500 cm^{-1}, this quantity corresponds mostly to the intensity of the nonresonant signal at each spatial position. Since the nonresonant signal depends on the local polarizability, it can be a good
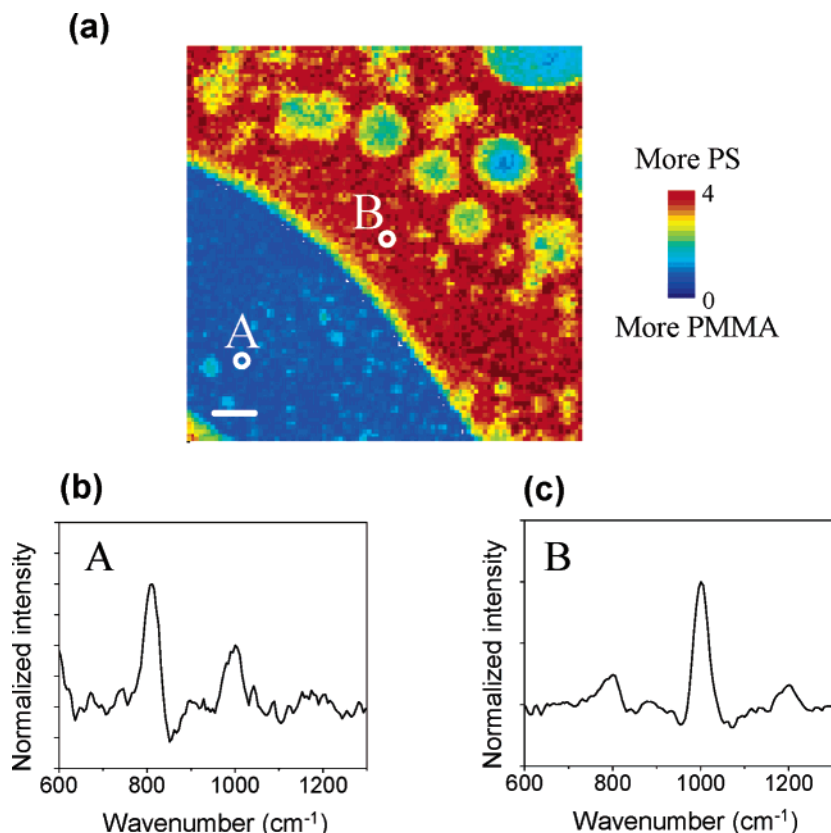
(a)

(b)

(c)

Figure 10. Chemical imaging of a polystyrene (PS)/poly(methyl methacrylate) (PMMA) mixture film. (a) Microscopic image constructed by the relative peak ratio between 1000 and 800 cm^{-1}. The color scale is from the relative peak ratio of 1000 cm^{-1}/800 cm^{-1}. The scale bar is 4 μm. The pixel size in the image is 400 nm $\times$ 400 nm. The DQSI-CARS spectra at (b) location A and (c) location B marked in panel a. (b and c) The two spectra of the actual microscopic data. The image in panel a is constructed with 10 000 such spectral data.

contrast mechanism for polarizability and morphology changes, similar to third harmonic generation (THG) microscopy.[24] This gives a better signal-to-noise ratio in the microscopy image due to the orders of magnitude larger nonresonant signal levels than the resonant signals. However, this signal does not permit chemical contrast. We can use this image as a guide (topology and polarizability mapping) for samples with weak signals to find interesting spatial locations and to do longer scan(s) to measure the resonant CARS spectrum. Panels c and d of Figure 9 are the chemical images constructed by the characteristic peaks of the PDMS (460 cm^{-1}) and amide (830 cm^{-1}). All images are scanned with a data acquisition time of 10 ms per pixel. In this case one pixel is 200 nm. We integrate the peak intensity over $\sim$60 cm^{-1} centered at the peak (note that the current spectral resolution is $\sim$35 cm^{-1}) after removing the background by subtracting a mean value at the two ends of the defined bandwidth of 60 cm^{-1} at each spectral data point. One can see that the contrast is reversed between the two images. In Figure 9c, the brighter contrast corresponds to the concentration of the PDMS, while in Figure 9d it corresponds to the amide. The amide has the same topography of the TEM copper grid and the PDMS has the opposite (negative) shape.

In a sample with chemical species that have overlapping CARS peaks it is not straightforward to apply the single peak imaging method demonstrated above. However, we can use spectral analysis to probe the local chemical identity. Figure 10a shows the chemical image of a spin cast film of a PS/PMMA mixture. We choose this sample for the demonstration, since PS and PMMA are known to phase-separate when cast into a film,[25] but both chemicals have peaks at similar positions (800 and 1000 cm^{-1}) in the present CARS window and similar spectral resolution. Thus, the single peak images,
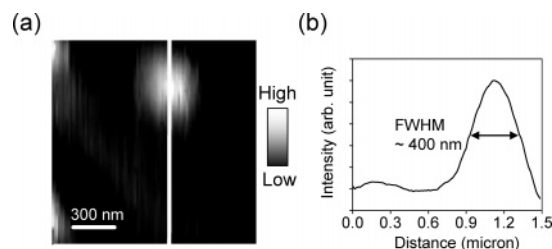
(a)　　　　　　　**(b)**

Figure 11. 11. (a) Total nonlinear signal image of a PMMA bead (200 nm diameter). The image size is 1.5 μm $\times$ 1.5 μm. The pixel size in the image is 15 nm $\times$ 15 nm. (b) A line profile plot of the vertical cut-line shown in panel a.

such as in Figure 9c,d, are not appropriate for chemical mapping. Here the relative intensity of the two peaks is used as the contrast mechanism. Again we use a 60 cm^{-1} integration bandwidth centered at 800 and 1000 cm^{-1} and remove background by subtracting a mean value of two points at the ends of the 60 cm^{-1} bandwidth to calculate the peak intensity. In PS, the relative peak ratio (1000 cm^{-1}/800 cm^{-1}) is $\sim$4 (Figure 10b), while in PMMA it is $\sim$0.5 (Figure 10c). The color code is proportional to this peak ratio and directly related to the local chemical identity. One can see that PS-rich (upper right) and PMMA-rich (lower left) regions are separated nicely and there are some areas exhibiting a mixture and segregation of both chemicals in Figure 10a.

Figure 11a shows the total nonlinear signal image from a PMMA bead (200 nm diameter, Polyscience) attached to a glass coverslip. In Figure 11b, the profile plot of the marked cut-line in Figure 11a is shown. The full width at half-maximum (fwhm) is $\sim$400 nm and the estimated point spread function has a fwhm of $(400^2 - 100^2)^{1/2} \approx 390$ nm assuming Gaussian distributions

Lim et al.

of the PMMA bead signals and beam profiles.[4] This spatial resolution is worse than a theoretical estimate of 230 nm, which is calculated for a 1.2 N.A., three-photon process and a diffraction-limited spot size from 800 nm wavelength. This discrepancy between the experimental and theoretical spatial resolutions can be attributed to various chromatic and achromatic aberrations, especially due to the broad bandwidth of the laser spectrum used in this paper. In other CARS reports, better spatial resolutions (<300 nm) have been demonstrated.[3,4]

Depolarization of signals by a scattering sample is a problem in any polarization-based technique. In Silberberg's original polarization and phase-controlled CARS method,[19] if a small amount of the signal is depolarized, the weak resonant signal is dominated by the leakage of an orders-of-magnitude larger nonresonant background. The shot noise from this background can easily obscure the resonant signal. In DQSI-CARS, the depolarization will also distort the spectral line shape and the baseline. Nevertheless, the shot noise from the local oscillator is already included in the resulting spectra (the function D, eq 13) and makes no change in the S/N ratio. The effect is similar to a nonpure local oscillator, i.e., distortion of the line shape. Therefore, DQSI-CARS is more tolerant to sample depolarization than the original polarization and phase-controlled CARS method.

There are some remaining issues to be solved, not just in our technique but also in a general multiplex CARS experiment.[2,5] First, the axial chromatic aberration (ACA) of the microscope objective can be a significant problem.[9] We have tested several objectives and find that one IR objective (1.2 N.A. water immersion microscope objective, Olympus) has the least ACA within the present bandwidth of the laser. This is verified by looking at the relative intensities of the high-frequency vibrational peaks to the lower frequency ones. If one has significant ACA at the focus, it will show up as weaker relative signal intensities in the higher vibrational frequency peaks. If one wishes to use an objective with a significant ACA (for example, a special objective having a long working distance), the ACA has to be compensated before the microscope setup.[9] Second, the bandwidth of the laser is still not broad enough to cover the entire fingerprint region. We can detect vibrational peaks from 400 to 1500 cm^{-1}, but the signal intensity decreases rapidly beyond 1200 cm^{-1}. The use of an oscillator with negatively chirped mirrors instead of prism pairs can provide much larger bandwidth, which covers the entire CARS vibrational spectral range,[26] but issues such as ACA and pulse compression with this large bandwidth have to be solved first.

Currently the sensitivity limit is that shown for the samples in Figure 8 with 10 ms experiment time. The sensitivity can be improved further by several approaches. First, if the available laser power is high enough, one can focus the laser pulse to a line, not a spot,[27] then image the entire line of spectra to a CCD to collect a significantly greater signal with a given time. Adopting this concept to DQSI-CARS can improve the sensitivity significantly. Second, the nonresonant signal will be greater with excitation by a broader bandwidth laser. With a larger local oscillator field, the amplification of the resonant signal will be enhanced. However, the pulse dispersion and ACA by a microscope objective has to be carefully corrected for such a pulse.

Here we demonstrated chemically selective microscopy by two simple methods: peak intensity and peak ratio imaging. A full spectral analysis with a known Raman spectrum will be more informative for chemical selectivity than single peak analysis. Even if there are no known Raman spectroscopic data,

or if complicated chemical identities at a spatial location make the assignment difficult, a linear discrimination analysis can be applied to classify the similarity between spatial positions.[28]

V. Conclusion

In this paper, we demonstrated a number of results with a new interferometric CARS spectroscopy technique, which can extract a background free vibrational CARS spectrum with single laser pulses and amplify the resonant CARS signals via a homodyne mixing with the nonresonant signal as the local oscillator. It has a simple and very stable experimental setup. We verify chemically selective microscopy using the vibrational spectrum itself as the contrast mechanism. This new technique enhances the signal sensitivity significantly and removes the nonresonant background problem in CARS microscopy. It can be readily applied to most microscopic samples in material and biological studies.

References and Notes

(1) Cheng, J. X.; Xie, X. S. *J. Phys. Chem. B* **2004**, *108*, 827.
(2) Muller, M.; Schins, J. M. *J. Phys. Chem. B* **2002**, *106*, 3715.
(3) Potma, E. O.; Xie, X. S.; Muntean, L.; Preusser, J.; Jones, D.; Ye, J.; Leone, S. R.; Hinsberg, W. D.; Schade, W. *J. Phys. Chem. B* **2004**, *108*, 1296.
(4) Zumbusch, A.; Holtom, G. R.; Xie, X. S. *Phys. Rev. Lett.* **1999**, *82*, 4142.
(5) Cheng, J. X.; Volkmer, A.; Book, L. D.; Xie, X. S. *J. Phys. Chem. B* **2002**, *106*, 8493.
(6) Levenson, M. D.; Kano, S. S. *Introduction to Nonlinear spectroscopy*; Academic Press: San Diego, CA, 1988.
(7) Dudovich, N.; Oron, D.; Silberberg, Y. *J. Chem. Phys.* **2003**, *118*, 9208.
(8) Wurpel, G. W. H.; Schins, J. M.; Muller, M. *J. Phys. Chem. B* **2004**, *108*, 3400.
(9) Kee, T. W.; Cicerone, M. T. *Opt. Lett.* **2004**, *29*, 2701.
(10) Lin-Vien, D.; Colthup, N. B.; Fateley, W. G.; Grasselli, J. G. *The Handbook of Infrared and Raman Characteristic Frequencies of Organic Molecules*; Academic Press: San Diego, CA, 1991.
(11) Oron, D.; Dudovich, N.; Silberberg, Y. *Phys. Rev. Lett.* **2002**, *89*, 273001.
(12) Lim, S.-H.; Caster, A. G.; Leone, S. R. *Phys. Rev. A* **2005**, *72*, 041803.
(13) Evans, C. L.; Potma, E. O.; Xie, X. S. *Opt. Lett.* **2004**, *29*, 2923.
(14) Marks, D. L.; Vinegoni, C.; Bredfeldt, J. S.; Boppart, S. A. *Appl. Phys. Lett.* **2004**, *85*, 5787.
(15) Marks, D. L.; Boppart, S. A. *Phys. Rev. Lett.* **2004**, *92*, 123905.
(16) Dudovich, N.; Oron, D.; Silberberg, Y. *Nature* **2002**, *418*, 523.
(17) Oron, D.; Dudovich, N.; Yelin, D.; Silberberg, Y. *Phys. Rev. Lett.* **2002**, *88*, 063004.
(18) Oron, D.; Dudovich, N.; Yelin, D.; Silberberg, Y. *Phys. Rev. A* **2002**, *65*, 043408.
(19) Oron, D.; Dudovich, N.; Silberberg, Y. *Phys. Rev. Lett.* **2003**, *90*, 213902.
(20) Lepetit, L.; Cheriaux, G.; Joffre, M. *J. Opt. Soc. Am. B* **1995**, *12*, 2467.
(21) Lozovoy, V. V.; Pastirk, I.; Dantus, M. *Opt. Lett.* **2004**, *29*, 775.
(22) Delong, K. W.; Trebino, R.; Hunter, J.; White, W. E. *J. Opt. Soc. Am. B* **1994**, *11*, 2206.
(23) Xia, Y.; Whitesides, G. M. *Annu. Rev. Mater. Sci.* **1998**, *28*, 153.
(24) Oron, D.; Yelin, D.; Tal, E.; Raz, S.; Fachima, R.; Silberberg, Y. *J. Struct. Biolo.* **2003**, *147*, 3.
(25) Johnson, W. C.; Wang, J.; Chen, Z. *J. Chem. Phys. B* **2005**, *109*, 6280.
(26) Venteon, Nanolayers Inc.
(27) Oron, D.; Silberberg, Y. *J. Opt. Soc. Am. B* **2004**, *21*, 1964.
(28) Schut, T. C. B.; Wolthuis, R.; Caspers, P. J.; Puppels, G. J. *J. Raman Spectrosc.* **2002**, *33*, 580.